

# Simulation of Self-Piercing Rivet Insertion Using Smoothed Particle Galerkin Method

Li Huang<sup>1</sup>, Youcai Wu<sup>2</sup>, Garret Huff<sup>3</sup>, Shiyao Huang<sup>1</sup>,  
Andrey Ilinich<sup>3</sup>, Amanda Freis<sup>3</sup>, George Luckey<sup>3</sup>

<sup>1</sup>Materials and Process Research, Ford Motor Research and Engineering Center,  
Nanjing, Jiangsu, 211100, China

<sup>2</sup>Livermore Software Technology Corporation, 7374 Las Positas Rd., Livermore, CA 94551, USA

<sup>3</sup>Research and Advanced Engineering Center, Ford Motor Company, Dearborn, MI 48121, USA

## Abstract

Self-piercing rivets (SPR) are efficient and economical joining elements for lightweight automotive body structures. In this paper, a meshfree Smoothed Particle Galerkin (SPG) method was applied to the simulation of the SPR insertion process. Two layers of aluminum alloy 6111-T4 were joined using a full three-dimensional (3D) model with LS-DYNA® explicit. The severely deformed upper sheet was modeled using the SPG method with activated bond failure, while the rest of the model was modeled using the traditional finite element approach. An extensive sensitivity study was conducted to evaluate the proposed approach, including bond failure criteria, kernel update frequency, kernel support size, mesh refinement, etc. The numerical results were compared to experimental data to demonstrate the robustness and effectiveness of the present method.

**Keywords:** Smoothed Particle Galerkin (SPG); self-piercing rivet (SPR); Meshfree

## 1. Introduction

The demand for lighter vehicles requires alternative materials in vehicle body structures, such as aluminum, magnesium or non-metals. Traditional welding techniques have some inherent challenges in dissimilar metal joining, and alternative solutions are needed to join these materials. Riveting is a direction-dependent mechanical joining technique, which enables mixed-material construction with a short cycle time. The SPR insertion process can be divided into four steps: clamping, piercing, flaring, and releasing, as shown in Fig. 1. The difference between an SPR and a conventional blind rivet is that an SPR does not require pre-drilled holes, and therefore the technology brings great benefits in terms of production cost reduction and ease of automation.

Given many possible rivet-die combinations available in the SPR joint design space, it can be a challenge to select a robust combination for each unique joint. However, the challenge is greater to find a single rivet-die combination suitable for multiple stack-ups. The traditional SPR joint development process is based on trial-and-error experiments and engineering experience. As such, development may require many samples to test a variety of combinations, and a numerical simulation of the riveting process could significantly boost efficiency.

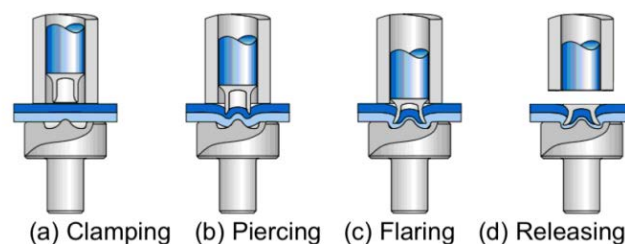


Fig. 1 Self-piercing rivet insertion process [1].

In 1997, King et al [2] created the first finite element model for SPR process in DEFORM-2D. Today, extensive research has improved the robustness and accuracy of SPR process modeling including material constitutive models, fracture criteria, interfacial friction profiles, contact settings etc. [3, 4]. Various commercial software packages have been used for SPR process simulation, including LS-DYNA, ABAQUS/Explicit, MSC.Simufact and DEFORM-2D etc. Most of the existing SPR insertion simulations implemented two-dimensional (2D) axisymmetric models [5-10] for simplicity, while full or partial 3D models [11] are under development. Such models have inherent numerical issues such as element distortion caused by large deformation and contact instability with broken surfaces.

Despite the academic progress of SPR process modelling, a huge gap remains before CAE could replace physical tests. Two key issues are the extreme deformation and subsequent material failure during the SPR process, and their computationally stable and efficient management. The piercing step requires material fracture, which can be modeled by either geometrical or physical criteria. For the geometrical criterion, the upper layer minimum thickness, at which the sheet would separate, needs to be defined. The mesh separation can be accomplished automatically [10] or manually [5, 12]. The physical criteria are typically elemental and based on metrics derived from stress and strain tensors [7] or phenomenological damage [6]. The fracture is initiated and propagated by element deletion, which results in non-real energy and volume loss. Alternatively, a node decoupling can be used where coupled nodes need to be disconnected to create an artificial cracking path known a priori, which clearly cannot be accomplished for novel stack-ups or materials. Element distortion is another barrier that limits the accuracy and robustness of the simulation because of severe material deformation, especially around the rivet tip. The mesh distortion can be partly eliminated by adaptive re-meshing [14], which cyclically refines the mesh to improve the element quality at a given frequency. However, the re-meshing technique might introduce significant numerical errors during state and field variable mapping, depending on the mapping frequency and element size, and result in inconsistent SPR cross-section predictions in 2D axisymmetric simulation [10]. 3D adaptive re-meshing is not numerically stable in current commercial solvers.

Meshfree or meshless methods construct approximation functions based on discrete nodes and do not require connections between nodes within the simulation domain. They offer numerous advantages over the conventional finite element method (FEM) in the modeling of large material deformation, moving strong discontinuities, and immersed structures [15]. Meshfree approaches have been developed in the past several decades, and have become increasingly applicable to simulate both fluid flow and solid mechanics applications. However, numerical instabilities, such as tension instability [16], spurious energy mode [17], and particle support related convergence [18], are encountered in the application of meshfree methods. Current approaches to suppress these instabilities require either sophisticated stabilization control parameters [17] or background mesh in nodal integration [12, 19], which significantly limit their applications in simulating destructive manufacturing such as metal grinding, drilling, and riveting. Recently, Wu et. al [15, 20-22] developed the Smoothed Particle Galerkin (SPG) method using the direct nodal integration (DNI) technique. A strain operator derived from displacement smoothing theory was utilized to stabilize the DNI scheme without ad-hoc parameters. An adaptive anisotropic Lagrangian kernel [22] was implemented into the SPG method to deal with large deformation and suppress tension instability. The Lagrangian kernel is updated constantly over a period of time to capture the large deformation. The material derivatives of meshfree shape functions are always computed and stored for the new reference configuration at the end of each time step. Since this particle-based reconstruction step does not involve re-meshing, the stress-recovery techniques or remapping procedures are unnecessary and hence better accuracy can be achieved. Additionally, due to the strain gradient stabilization technique in the SPG method, grinding and shearing problems [15, 20] have been found insensitive to SPG support sizes and mesh discretization. Detailed formulations of the SPG method can be found in literature [15, 21, 22].

In the SPG method, a bond-based failure criterion [21] was implemented to avoid excessive strain. In this failure criterion, two neighbored particles are disconnected after their averaged effective plastic strain  $\epsilon_{eff}^p$  reaches a user-defined critical value. In particular, the kinematic bond between particle 1 and particle 2, shown as the black dashed line in Fig. 2, is removed when the averaged effective plastic strain  $\epsilon_{12}^p$  reaches the critical value so that particle 2 is not involved in the computation of deformation gradient at particle 1, and vice versa.

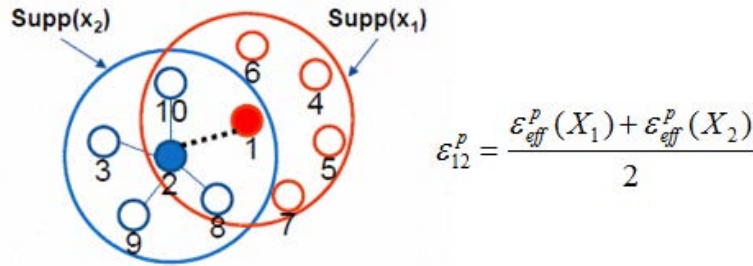


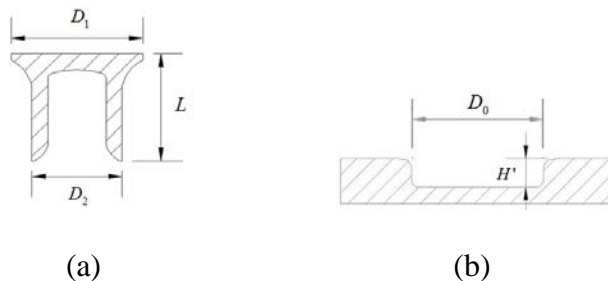
Fig. 2 The bond-based failure in SPG.

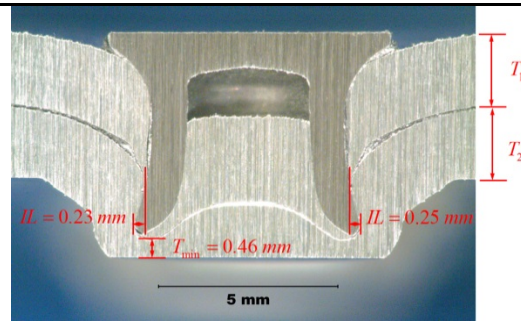
Additionally, the SPG method can be coupled with Lagrangian FEM within the same model to improve computational efficiency [15]. The feasibility of hybrid SPG-FEM models was investigated and confirmed in prior research [15, 20-22].

This paper presents an alternative approach of 3D SPR insertion process simulation with the SPG method. Numerical simulations were performed using LS-DYNA/explicit and compared to test results. The rest of the paper is organized as follows: the experimental setup and material properties are introduced in Section 2; the hybrid SPG and FEM modeling strategy is presented in Section 3; the simulation results are discussed and compared with test results in Section 4; and conclusions are made in Section 5.

## 2. Experiments and Material Properties

In the present research, a stack-up of two layers of 2.0 mm thick AA6111-T4 sheet were riveted by a Henrob servo-electric SPR gun. The countersunk rivets were made from boron steel. The rivet and die geometries are illustrated in Fig. 3(a) and Fig. 3(b), respectively. The cross-section profile of the SPR joint is shown in Fig. 3(c). Two key characteristics were measured, the remaining material thickness ( $T_{min}$ ) and the rivet interlock ( $IL$ ).  $T_{min}$  is defined as the thinnest part of the plastically deformed material on the die side, and  $IL$  is defined as the distance between the left / right rivet leg tip and the center-most captured point of the lower material in the joint. Table 1 summarizes the basic characteristic dimensions: rivet length  $L$ , head diameter  $D_1$ , and shank diameter  $D_2$ , while the die has two key variables: die diameter  $D_0$ , and die depth  $H'$ .





(c)

Fig. 3 Geometry of the (a) rivet and (b) die, and (c) resulting cross-section image of SPR joint made from two layers of 2.0mm thick AA6111-T4.

Basic material properties are listed in Table 2, where  $E$  is the young's modulus;  $\sigma_{0.2}$  is the yield stress;  $E_t$  is the tangent modulus;  $K$  is the strength coefficient and  $n$  is the hardening exponent for the power law. Since aluminum alloys typically have low strain rate sensitivity at room temperature as a face centered cubic (FCC) metal, strain rate effect was not considered in this study. The rivet material properties were obtained from lateral compression tests of rivet shank [7].

Table 1 Dimensions of Rivet and Die

Top sheet		Bottom sheet		Rivet			Die	
$T_1$ (mm)	$T_2$ (mm)	$D_1$ (mm)	$D_2$ (mm)	$L$ (mm)	$D_0$ (mm)	$H'$ (mm)		
2.0	2.0	7.8	5.3	6.5	10	2.2		

Table 2 Summary of Basic Material Properties[7]

Material	$E$ (Gpa)	$\sigma_{0.2}$ (Mpa)	$E_t$	$K$	$n$
AA 6111-T4	70	135	-	408	0.18
Rivet	210	1750	1650	-	-

### 3. Numerical Modeling

A hybrid SPG-FEM model, shown in Fig. 4, was created in this work to save computational cost. In this 3D model, the punch, blank holder and die were treated as rigid, while the rivet and work pieces were modeled as elastic-plastic materials. The center portion of the top sheet where large deformation and material fracture occurs was modeled using SPG particles, while all the other remaining parts were modeled by FEM to avoid excessive increase of computational cost. The parameters of the baseline model are given in Table 3. In this model, the particle distance was 0.2mm, and the normalized nodal support size was set to 1.6 to define the influence domain of each particle. An updated Lagrangian kernel was adopted as the kernel approximation with updates performed every 20 explicit time steps.

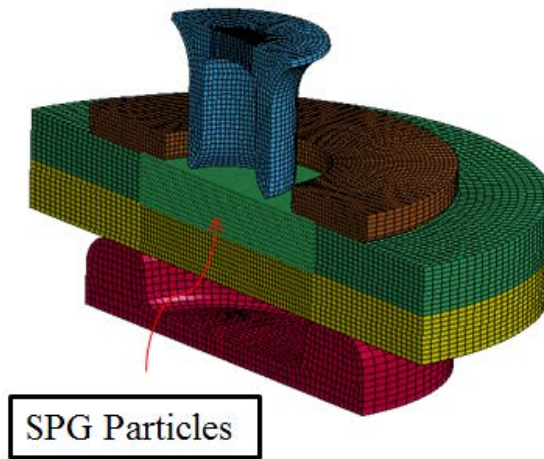
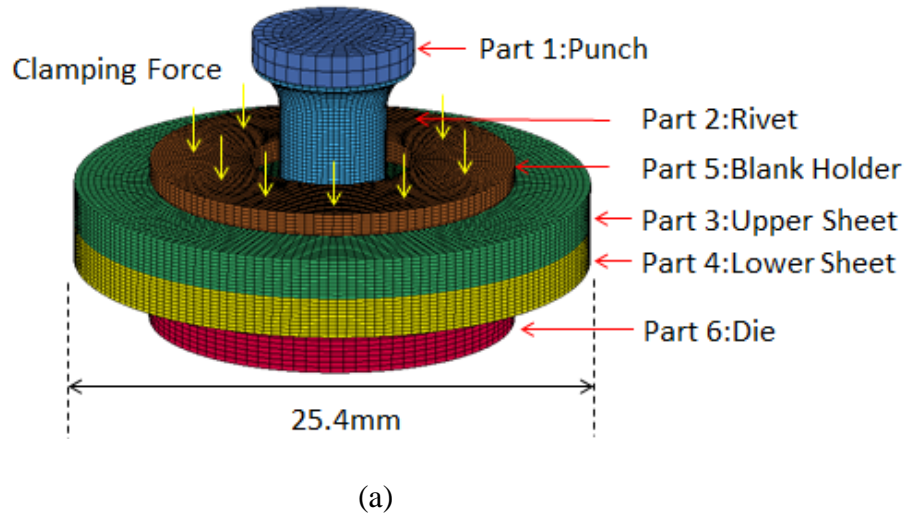


Fig. 4 Hybrid FEM-SPG model for SPR simulation (a) Full 3D model (b) Center portion of the top sheet modeled by SPG.

Table 3 Summary of Baseline Model Parameters

Top sheet – the center portion	SPG, elastic-plastic with bond failure
Top sheet – the outer portion	FEM, elastic-plastic
Rivet and bottom sheet	FEM, elastic-plastic
Punch, blank holder and die	FEM, rigid
SPG particle distance (mm)	0.2
FEM element size (deformable) (mm)	0.2
Blank holder force (kN)	3
Riveting speed (mm/s)	130
Coefficient of friction at interfaces	0.2
SPG kernel update frequency	20
Mass scaling factor	10000

The work pieces were clamped with constant blank holder force of 3 kN throughout the riveting process, and free boundary condition was applied at the outer edge. The punch was assigned a constant velocity of 130mm/s to make the total riveting time consistent with the real application. The constant velocity profile was selected for simplicity and likely had minimal impact on prediction accuracy due to the rate insensitive material model. The simulation was terminated once the rivet head became flush to the upper sheet surface. The standard node to surface contact algorithm was adopted between the SPG particles and the rivet, and between the SPG particles and bottom sheet, while the surface to surface contact algorithm was adopted for all other contact pairs. The coefficient of friction (CF) was fixed at 0.2 for both static and dynamic contacts at all interfaces. Mass scaling was implemented to increase the explicit time step and reduce CPU time.

The SPG bond-based failure criterion was applied in the model. The critical effective plastic strain for bond failure was set at 0.54 based on the previous experimental data for AA6111-T4 [7]. Additionally, a bond stretching condition was applied to prevent failure in compression which is uncommon in metals. In particular, this condition permitted bond failure only when the ratio between the current and initial distance of the paired particles was larger than unity.

Table 4 Sensitivity Study of Modeling Parameters

	SPG Particle Distance (mm)	Bond-based Fracture Strain	Nodal Support Size	Kernel Update Frequency	Mass Scale Factor	Yield Stress Scale Factor
Model A (Baseline)	0.2	0.54	1.6	20	10000	1
Model B	0.2	0.54	1.6	20	1000	1
Model C	0.2	0.54	1.6	20	500	1
Model D	0.2	1	1.6	20	10000	1
Model E	0.2	2	1.6	20	10000	1
Model F	0.2	0.54	1.4	20	10000	1
Model G	0.2	0.54	1.8	20	10000	1
Model H	0.2	0.54	1.6	10	10000	1
Model I	0.2	0.54	1.6	30	10000	1
Model J	0.1	0.54	1.6	20	10000	1
Model K	0.2	0.54	1.6	20	10000	1.2
Model L	0.2	0.54	1.6	20	10000	1.5

To understand the feasibility of the proposed approach, sensitivity study of model parameters, including bond failure criteria, kernel update frequency, kernel support size, mesh refinement, and mass scaling was performed according to the matrix listed in Table 4.

#### 4. Result and Discussion

The cross-section profile predicted by the baseline model (Model A) is compared to the experimental cross-section in Fig. 5. The model accurately predicted all geometrical features except the shape of the slug within the rivet bore. This deviation could be partially explained by an overly-stiff response of bottom sheet during penetration of rivet tail. Possible solutions could be to find a viable way to reduce element distortion or introduce similar meshfree approach for the bottom sheet, which will be addressed in future work. In summary, the material separation and flow was replicated well by the SPG model. More importantly, large deformation and fracture were simulated successfully without any artificial stabilization or parameter tuning.

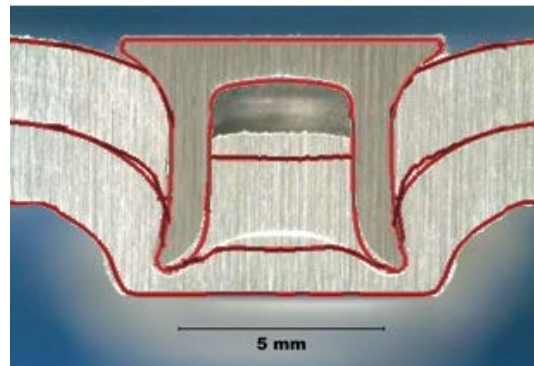


Fig. 5 Comparison of the cross-section profile between simulation and test (the contour lines represent simulation results)

Four intermediary steps during simulated SPR insertion are given in Fig. 6 with von Mises stress and effective strain distributions. The stresses (Fig. 6a) and strains (Fig. 6b) were concentrated near the rivet tip and the bottom part of the lower sheet. The SPG particles in the center portion of the top sheet flowed and separated naturally and smoothly. A small amount of material from the top sheet could be severely compressed under the rivet tip. The severe deformation in this area is typically very challenging to model by conventional FEM, but it was well captured by the SPG method. Since element erosion was avoided, the unphysical volume and energy loss was prevented during the riveting simulation, which is critical to accurately predict punch force and cross-section profile.

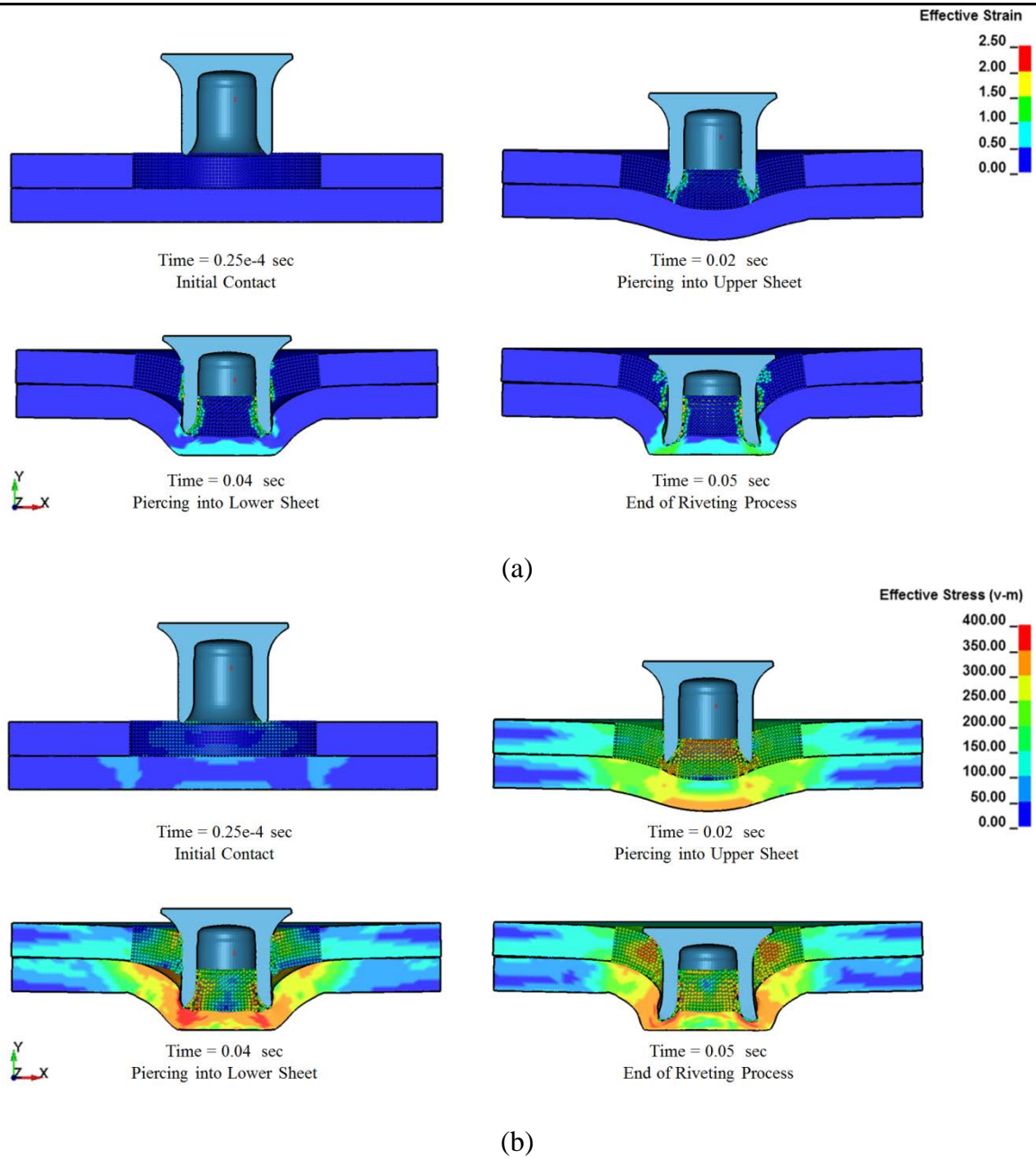


Fig. 6 Distribution of field variables during SPR insertion: (a) evolution of effective strain, (b) evolution of Mises stress (MPa).

Punch force curves and critical geometrical dimensions predicted by different models in the parameter sensitivity study are compared in Fig. 7 and Table 5 respectively. It can be seen that the SPR simulation results did not show significant sensitivity to the main SPG parameters: bond failure strain, kernel update frequency, kernel support size, particle distance, or mass scaling. The yield stress scale factor, on the other hand, had a significant influence on both the force and cross-section profile. Models with increased yield stress (Model K and L) demonstrated increased force response, more rivet tail expansion (larger  $IL$ ), and less rivet penetration into the bottom layer (higher  $T_{min}$ ). Overall, the sensitivity study highlighted the importance of obtaining accurate elastic-plastic properties, especially hardening for the joined materials and the rivet. It also demonstrated smaller sensitivity of the SPG model to fracture criterion parameters, which is a substantial advantage of this modelling method.

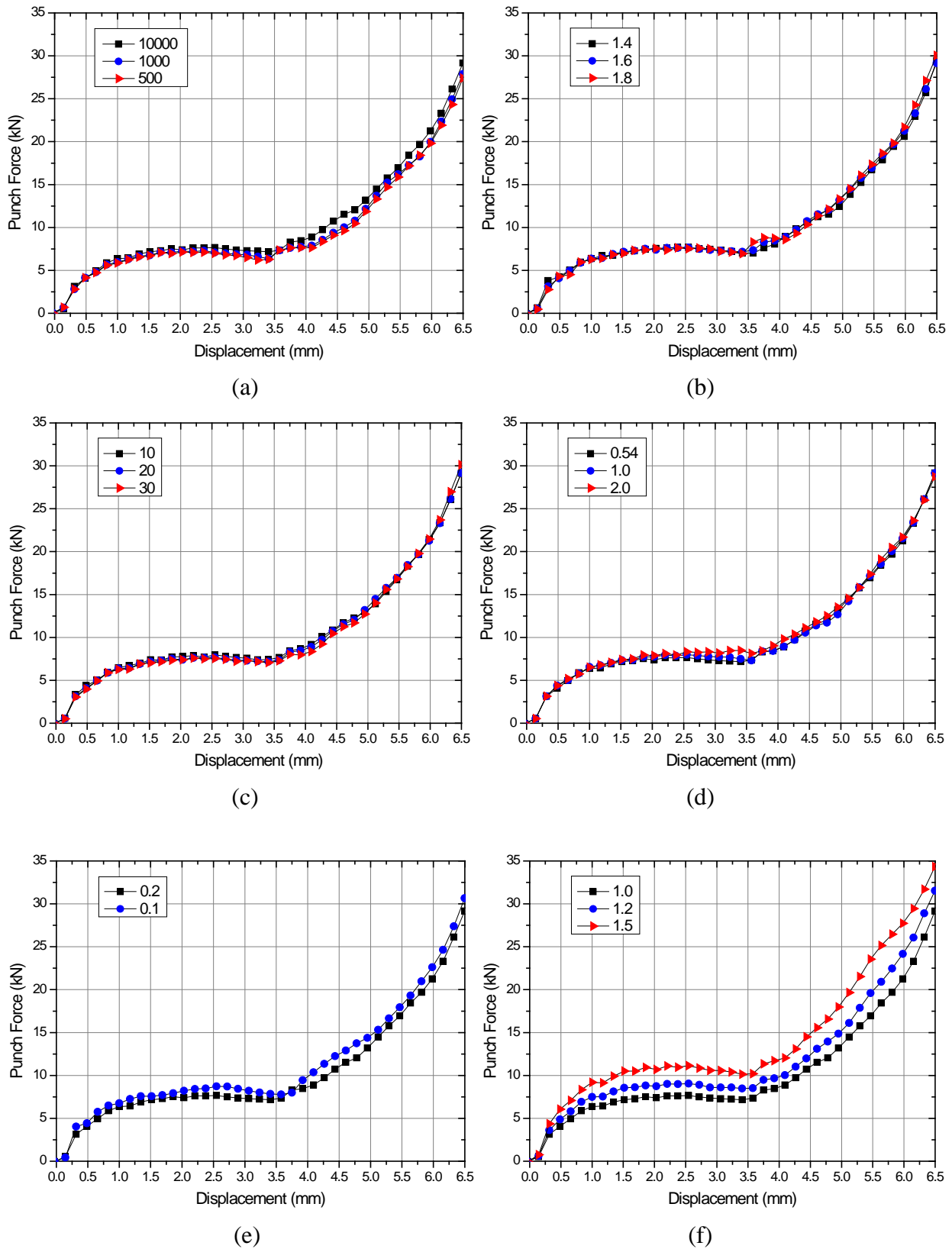


Fig. 7 Simulated force-displacement curves: (a) mass scaling factor, (b) SPG normalized support size, (c) SPG kernel update frequency, (d) SPG bond failure criterion, (e) SPG particle distance, (f) post-yield stress scale factor.

Table 5 Comparisons between predicted  $T_{\min}$  and  $IL$  values and measurements

	$T_{\min}$ (mm)	$IL$ (mm)
Experimental values	0.46	0.24
Model A (Baseline)	0.55	0.18
Model B	0.52	0.18
Model C	0.48	0.18
Model D	0.55	0.17
Model E	0.55	0.19
Model F	0.52	0.18
Model G	0.52	0.18
Model H	0.52	0.17
Model I	0.54	0.18
Model J	0.51	0.15
Model K	0.61	0.22
Model L	0.72	0.32

## 5. Summary

This paper described a new numerical methodology, e.g. SPG, to simulate the SPR insertion process using a hybrid SPG-FEM 3D model. To keep the balance between computational cost and numerical accuracy, only the most severely deformed region was modeled by SPG, while the rest of the model was FEM based. A reasonable agreement between the simulation and experiment has been achieved in terms of cross-sectional profile, while stable punch-force responses were obtained. In SPG, the adaptive Lagrangian kernel successfully captured the large deformation without ad-hoc stabilization parameters. A bond-based failure criterion was introduced to model fracture with reduced discretization scale sensitivity while avoiding the usage of element erosion. It is important to note that the simulation results did not show significant sensitivity to the main SPG parameters: bond failure criterion, kernel update frequency, kernel support size, particle distance, or mass scale. The presented method offers an attractive way to process virtual manufacturing, and could be extended to other complex joining processes such as flow drill screwing (FDS) and friction stir welding (FSW). Additionally, the 3D nature of the presented model enables investigation of parameters that are impossible to study using the conventional 2D axisymmetric models, such as rivet insertion angle and rivet asymmetry.

## References

- [1] Self-pierce riveting for perfect joints, Boellhoff cooperation, (2010).
- [2] R.P. King, J.M. O'Sullivan, D. Spurgeon, P. Bentley, Setting load requirements and fastening strength in the self-pierce riveting process, in: Proceedings of the 11th National Conference on Manufacturing Research, 1995, pp. 57-61.
- [3] D. Li, A. Chrysanthou, I. Patel, G. Williams, Self-piercing riveting-a review, The International Journal of Advanced Manufacturing Technology, 92 (2017) 1777-1824.
- [4] X. He, F. Gu, A. Ball, Recent development in finite element analysis of self-piercing riveted joints, The international journal of advanced manufacturing technology, 58 (2012) 643-649.
- [5] B. Sui, B.H. Chang, D. Du, H. Huang, L. Wang, Simulation and analysis of self-piercing riveting process in aluminum sheets, Mater Sci Technol, 15 (2007) 713-717.
- [6] G. Casalino, A. Rotondo, A. Ludovico, On the numerical modelling of the multiphysics self piercing riveting process based on the finite element technique, Advances in Engineering Software, 39 (2008) 787-795.
- [7] L. Huang, J.V. Lasecki, H. Guo, X. Su, Finite element modeling of dissimilar metal self-piercing riveting process, SAE International Journal of Materials and Manufacturing, 7 (2014) 698-705.
- [8] L. Huang, J. Moraes, D.G. Sediako, J. Jordon, H. Guo, X. Su, Finite-Element and Residual Stress Analysis of Self-Pierce Riveting in Dissimilar Metal Sheets, Journal of Manufacturing Science and Engineering, 139 (2017) 021007, doi: 10.1115/1.4034437.
- [9] J.F.C. Moraes, J.B. Jordon, D.J. Bammann, Finite Element Analysis of Self-Pierce Riveting in Magnesium Alloys Sheets, Journal of Engineering Materials and Technology, 137 (2014) 021002, doi: 10.1115/1.4029032.
- [10] R. Porcaro, A.G. Hanssen, M. Langseth, A. Aalberg, Self-piercing riveting process: An experimental and numerical investigation, Journal of Materials Processing Technology, 171 (2006) 10-20.
- [11] J.F.C. Moraes, H.M. Rao, J.B. Jordon, M.E. Barkey, High cycle fatigue mechanisms of aluminum self-piercing riveted joints, Fatigue & Fracture of Engineering Materials & Structures, 41 (2018) 57-70.
- [12] W. Cai, H.-P. Wang, C.T. Wu, A coupled finite element/meshfree moving boundary method for self-piercing riveting simulation, Interaction and multiscale mechanics, 6 (2013) 257-270.
- [13] Y. Ma, Y. Li, W. Hu, M. Lou, Z. Lin, Modeling of friction self-piercing riveting of aluminum to magnesium, Journal of Manufacturing Science and Engineering, 138 (2016) 061007, doi: 10.1115/1.4032085.
- [14] LS-DYNA User's Manual Version 971, Livermore Software Technology Corporation, (2017).
- [15] C.T. Wu, T.Q. Bui, Y. Wu, T.-L. Luo, M. Wang, C.-C. Liao, P.-Y. Chen, Y.-S. Lai, Numerical and experimental validation of a particle Galerkin method for metal grinding simulation, Computational Mechanics, (2017) <https://doi.org/10.1007/s00466-017-1456-6>.
- [16] J. Swegle, D. Hicks, S. Attaway, Smoothed particle hydrodynamics stability analysis, Journal of computational physics, 116 (1995) 123-134.
- [17] S. Beissel, T. Belytschko, Nodal integration of the element-free Galerkin method, Computer methods in applied mechanics and engineering, 139 (1996) 49-74.
- [18] T. Belytschko, Y. Krongauz, J. Dolbow, C. Gerlach, On the completeness of meshfree particle methods, International Journal for Numerical Methods in Engineering, 43 (1998) 785-819.
- [19] J.S. Chen, C.T. Wu, S. Yoon, Y. You, A stabilized conforming nodal integration for Galerkin mesh-free methods, International journal for numerical methods in engineering, 50 (2001) 435-466.
- [20] C.T. Wu, M. Koishi, W. Hu, A displacement smoothing induced strain gradient stabilization for the meshfree Galerkin nodal integration method, Computational Mechanics, 56 (2015) 19-37.
- [21] C.T. Wu, Y. Wu, J.E. Crawford, J.M. Magallanes, Three-dimensional concrete impact and penetration simulations using the smoothed particle Galerkin method, International Journal of Impact Engineering, 106 (2017) 1-17.
- [22] C.T. Wu, S.W. Chi, M. Koishi, Y. Wu, Strain gradient stabilization with dual stress points for the meshfree nodal integration method in inelastic analyses, International Journal for Numerical Methods in Engineering, 107 (2016) 3-30.